Pure Appl. Geophys.

DOI 10.1007/s00024-014-0806-y

Pure and Applied Geophysics

Joint Inversion of Body-Wave Arrival Times and Surface-Wave Dispersion for Three-Dimensional Seismic Structure Around SAFOD

Haijiang Zhang,[1] Monica Maceira,[2] Philippe Roux,[3] and Clifford Thurber[4]

Abstract—We incorporate body-wave arrival time and surface-wave dispersion data into a joint inversion for three-dimensional P-wave and S-wave velocity structure of the crust surrounding the site of the San Andreas Fault Observatory at Depth. The contributions of the two data types to the inversion are controlled by the relative weighting of the respective equations. We find that the trade-off between fitting the two data types, controlled by the weighting, defines a clear optimal solution. Varying the weighting away from the optimal point leads to sharp increases in misfit for one data type with only modest reduction in misfit for the other data type. All the acceptable solutions yield structures with similar primary features, but the smaller-scale features change substantially. When there is a lower relative weight on the surface-wave data, it appears that the solution over-fits the body-wave data, leading to a relatively rough V_S model, whereas for the optimal weighting, we obtain a relatively smooth model that is able to fit both the body-wave and surface-wave observations adequately.

1. Introduction

The crust around the San Andreas Fault Observatory at Depth (SAFOD) has been the subject of many geophysical studies aimed at characterizing in detail the fault zone structure and elucidating the lithologies and physical properties of the surrounding rocks. Seismic methods in particular have revealed the complex two-dimensional (2D) and three-dimensional (3D) structure of the crustal volume around SAFOD (Lees and Malin, 1990; Michelini and McEvilly, 1991; Eberhart-Phillips and Michael, 1993; Thurber *et al.*, 2003, 2004; Hole *et al.*, 2006; Roecker *et al.*, 2006; Bleibinhaus *et al.*, 2007; Zhang *et al.*, 2005, 2009; Bennington *et al.*, 2008), and the strong velocity reduction in the fault damage zone (Li *et al.*, 1990, 1997, 2004; Ben Zion and Malin, 1991; Korneev *et al.*, 2003; Li and Malin, 2008; Lewis and Ben Zion, 2010; Wu *et al.*, 2010). Important additional insights have been obtained from magnetotelluric (MT) studies (Unsworth *et al.*, 1997, 2000; Unsworth and Bedrosian, 2004; Becken *et al.*, 2008), and some studies have carried out different types of joint geophysical inversion (Roecker *et al.*, 2004; Bennington *et al.* in revision).

Here, we experiment with a different type of joint inversion, using body-wave arrival time and surface-wave dispersion data to image the P-wave and S-wave velocity structure of the upper crust surrounding SAFOD. The two data types have complementary strengths—the body-wave data have good resolution at depth, albeit only where there are crossing rays between sources and receivers, whereas the short-period surface waves have very good near-surface resolution and are not dependent on the earthquake source distribution because they are derived from ambient noise. The body-wave data are from local earthquakes and explosions, comprising the dataset analyzed by Zhang *et al.* (2009). The surface-wave data are for Love waves from ambient noise correlations, and are from Roux *et al.* (2011). We examine how the S-wave model varies as we vary the relative weighting of the fit to the two data sets and in comparison to the previous separate inversion results, and assess whether the "optimal" model, based on the weight corresponding to the corner of a

[1] Laboratory of Seismology and Earth's Interior, School of Earth and Space Sciences, University of Science and Technology of China, 96 Jinzhai Road, Hefei 230026, Anhui, China. E-mail: zhang11@ustc.edu.cn

[2] Earth and Environmental Sciences, Los Alamos National Laboratory, Los Alamos, New Mexico 87545, USA.

[3] ISTerre, CNRS, IRD, Université Joseph Fourier, Saint-Martin-d'Hères, France.

[4] Department of Geoscience, University of Wisconsin-Madison, Madison, Wisconsin 53706, USA.

Published online: 29 March 2014

trade-off curve, indeed appears to be optimal or not. We note that due to the indirect coupling of the S-wave and P-wave models only through the hypocenter parameters, the P-wave models obtained with the different weights are virtually indistinguishable from each other and from the original model of ZHANG *et al.* (2009).

2. *Datasets and Processing*

Figure 1 shows a map of the events and stations from which body-wave arrival-time and surface-wave dispersion data were obtained (ZHANG *et al.*, 2009). The main source of data is a temporary seismic array known as the Parkfield Area Seismic Observatory (PASO) (THURBER *et al.*, 2003, 2004). All of the PASO array stations had three-component sensors with the majority of them being broadband. We also include data from (1) the UC-Berkeley High Resolution Seismic Network (HRSN), (2) fault-zone guided wave field projects in 1994 (LI *et al.*, 1997) and 2004 (LI and MALIN, 2008), (3) the USGS Central California Seismic Network, and (4) USGS temporary stations. Earthquake and explosion data were also obtained from borehole seismic strings deployed in the SAFOD Pilot Hole in July 2002 (CHAVARRIA *et al.*, 2003) and in the SAFOD main borehole in May 2005 by Paulsson Geophysical Services, Inc., as well as from borehole geophones deployed periodically in the SAFOD borehole between December 2004 and November 2006 by the SAFOD project. Sources of explosion data include a $\sim$5 km long high-resolution reflection/refraction line in 1998 (HOLE *et al.*, 2001; CATCHINGS *et al.*, 2002), a $\sim$50 km long reflection/refraction line in 2003 (HOLE *et al.*, 2006), and PASO "calibration" shots in 2002, 2003, 2004, and 2006. In total, there are 1,563 events including 574 earthquakes, 836 shots (explosions with known location and origin times), and 153 blasts (explosions with known location and uncertain origin times). There are about 90,800 arrival times (72 % P and 28 % S) included in the inversion. For the 574 earthquakes, differential times (approximately 489,000 P and 364,000 S) from event pairs observed at common stations were also calculated using a waveform cross-correlation package, BCSEIS (DU *et al.*, 2004).

The continuous data for the ambient noise analysis were obtained from 30 broadband stations of the PASO array (green triangles in Fig. 1). Since the local ambient seismic noise is dominated by the microseism noise excitation around 0.15 Hz (TANIMOTO *et al.*, 2006), the signals were pre-whitened between 0.15 and 0.35 Hz to allow an extension of the group velocity analysis to higher frequencies. For such directive noise (coming from the Pacific Ocean),

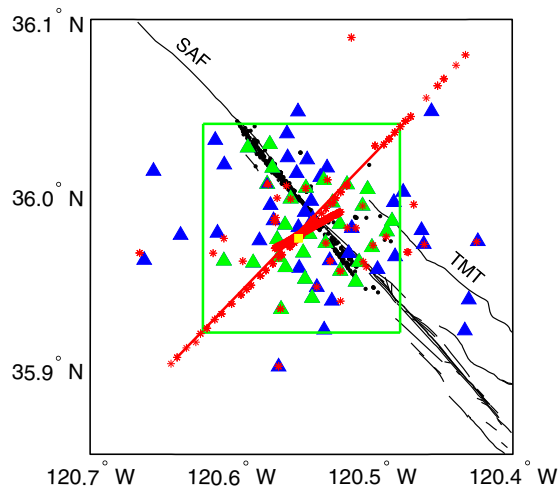

Figure 1
Map of seismicity (*black dots*), seismic stations (*triangles*), shots (*red stars*), and faults (*black lines*). The *green box* indicates the model volume shown in Fig. 6. *Green triangles* are the stations used for the surface-wave analysis. The *yellow square* indicates the SAFOD site. *SAF* San Andreas Fault, *TMT* Table Mountain Thrust

the concept of passive seismic-noise tomography was explored on three-component sensors (Roux *et al.*, 2011). An optimal rotation algorithm (ORA) was applied to the nine-component correlation tensor measured from each pair of three-component seismometers among the array, that forced each station pair to re-align in the noise direction, a necessary condition to extract unbiased travel-times from passive seismic processing (Roux, 2009; Roueff *et al.*, 2009). Taking advantage of the short distances between the sensors, only a relatively short time period of data (15 days) was needed to obtain adequate correlation results.

Note that no near-field contributions of the surface-wave's tensor were retrieved from the noise correlation, as the dominant noise source was in the far field. This confirmed that noise correlation on long time records simply behaves as a time-domain interferometer that magnifies phase coherence between station pairs in the frequency bandwidth of interest. As a consequence, the small size of the seismic network is both an advantage and a disadvantage regarding tomography inversion: an advantage as the coherence is high for many station pairs, which makes travel time measurements very accurate; a disadvantage since travel times extracted from the noise-correlation tensor are close to zero, which could make residual uncertainty of great importance in velocity measurement errors. In practice, an average signal-to-noise ratio of 60 was obtained at the peak maximum of the 15-day-averaged correlation function for each station pair. With such a high value of the signal-to-noise ratio, the accuracy of the travel-time measurement could, in theory, be close to infinity and, at least in practice, sufficiently high to provide reliable estimations.

Finally, after the rotation was performed, an optimal surface-wave tensor is obtained from which Rayleigh and Love waves were separately extracted for tomography inversion [see Fig. 2 and further details about the Love-wave inversion in Roux *et al.* (2011)]. The choice of Love waves for the inversion was motivated by (1) their high sensitivity to shallow geophysical structure and (2) the residual pollution of P-waves on the vertical and radial components (Roux *et al.*, 2005) of the correlation tensor that may bias the dispersion curve of Rayleigh waves. The tomography

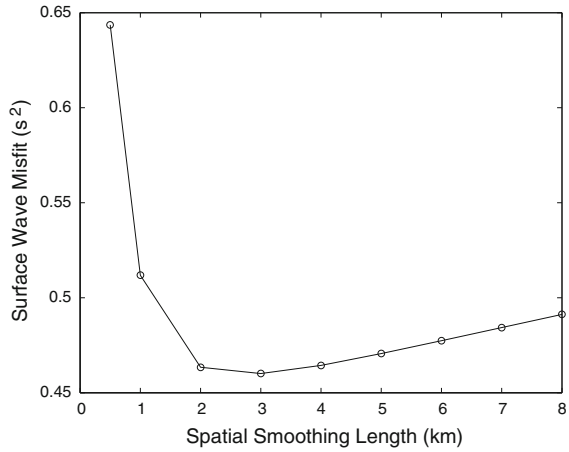

Figure 2
Example misfit *curve*, for the 0.3 Hz band, for the determination of the optimal spatial smoothing length for the Love wave group velocity maps of Roux *et al.* (2011) that are used in our joint inversion. The plot indicates the minimum falls between 2.0 and 3.0 km, so a value of 2.5 km was adopted

inversion resulted from the combination of 360 selected dispersion curves for Love waves. Straight rays were assumed as propagation paths and a 2.5-km spatial smoothing was applied. The latter was based on the point of minimum misfit as a function of spatial smoothing length (Fig. 2). This shows that the surface-wave group velocity maps were not heavily smoothed. Examples of group velocity maps from Roux *et al.* (2011) are shown in Fig. 3. The northeast-southwest velocity gradient across the San Andreas Fault (SAF) is clearly visible in the Roux *et al.* (2011) V_s model, as well as the low-velocity region down to $\sim$2.5 km below the surface between the SAFOD borehole and the SAF surface trace.

3. Joint Inversion

First, we describe the basic elements of the (separate) body-wave and surface-wave inversions that are incorporated into our joint inversion and then we explain how the joint inversion is set up.

For this work, we make use of the regional-scale version of the double-difference (DD) tomography algorithm tomoDD (Zhang and Thurber, 2003, 2006). DD tomography is a generalization of DD location (Waldhauser and Ellsworth, 2000), simultaneously solving for the 3D velocity structure and seismic event

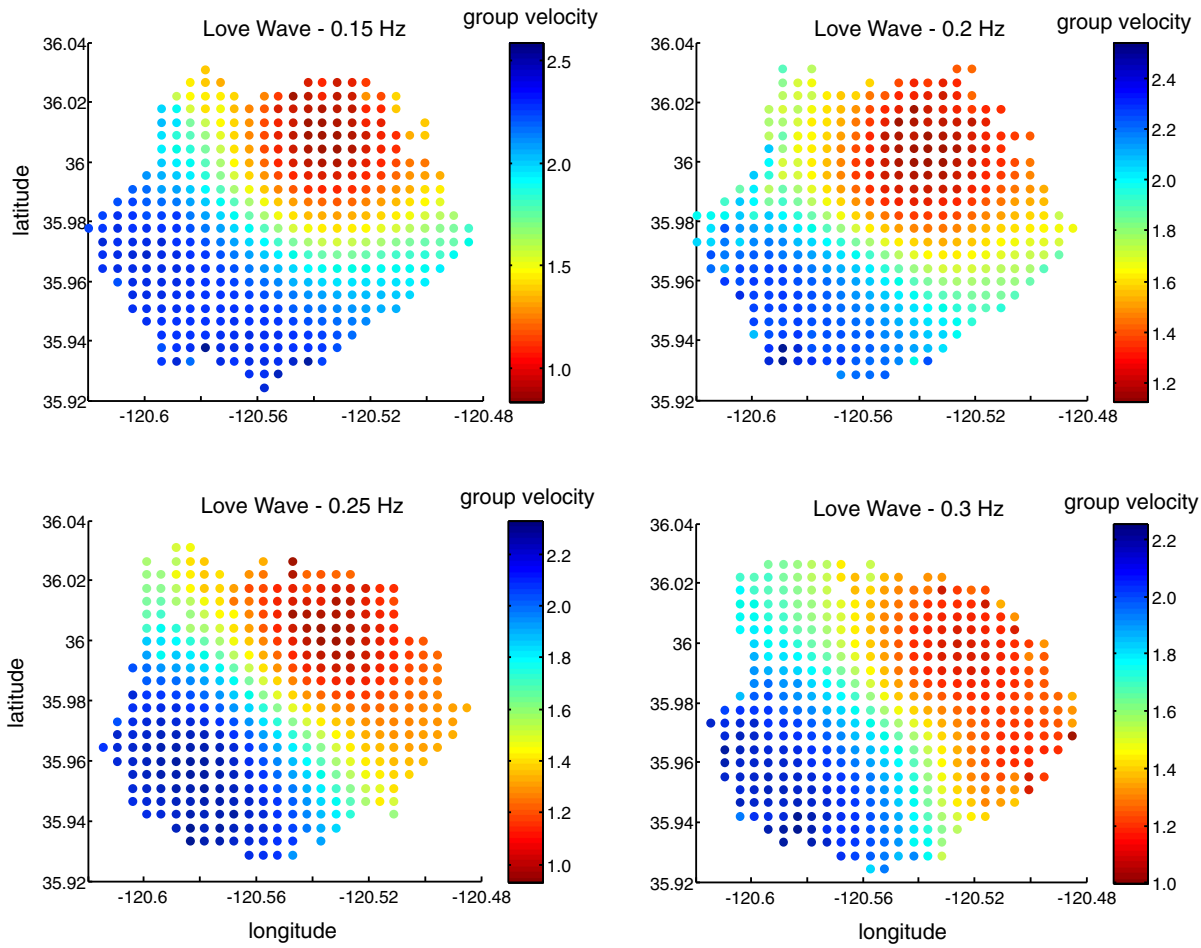

Figure 3
Example Love wave group velocity maps from Roux *et al.* (2011) used in our joint inversion. Velocities are in m/s

locations. The P-wave and S-wave velocity models are inverted for as separate models, although they are mathematically coupled through the hypocenter parameters. DD tomography uses a combination of absolute and more accurate differential arrival times and hierarchically determines the velocity structure from larger scale to smaller scale. LSQR (Paige and Saunders, 1982) is used to invert for model perturbations, and regularization of the inversion is accomplished with a first-difference smoothing operator. The regional-scale version, tomoFDD (Zhang *et al.*, 2004), employs a finite-difference solver [either Podvin and Lecomte (1991), or Hole and Zelt (1995), the latter based on Vidale (1988)] to calculate travel times in a spherical Earth geometry that is converted to a Cartesian system (so-called "sphere in a box").

The surface-wave inversion code that is integrated into the joint inversion algorithm is from Maceira and Ammon (2009) and follows Julià *et al.* (2000). The propagator matrix solver in the algorithm DISPER80 (Saito, 1988) is used for the forward calculation of dispersion curves from layered velocity models. Theoretically, the dispersion curve is a function of shear wave velocity, compressional wave velocity, and density of the media (Bucher and Smith, 1971). However, the sensitivity to P-wave velocity and density is significantly smaller than the sensitivity to S-wave velocity (Takeuchi and Saito, 1972; Aki and Richards, 1980; Bache *et al.*, 1978; Tanimoto, 1991). Therefore, only shear velocity variations are considered for modeling the Love wave dispersion observations.

To accomplish the joint inversion, the body-wave and surface-wave equations are combined in a single system with weighting factors controlling the relative contributions of the two data types to the solution for model perturbations. We note that, in general, the body-wave equations involve the P-wave and S-wave velocity structure and the source locations and/or origin times (for earthquakes and explosions with unknown origin time), whereas the surface-wave equations only involve the S-wave velocity. Thus, the joint inversion equations can be expressed as

$$\begin{bmatrix} \mu_1 \mathbf{G}_{\mathrm{H}}^{T_\mathrm{p}} & \mu_1 \mathbf{G}_{V_\mathrm{p}}^{T_\mathrm{p}} & \mathbf{0} \\ \mu_2 \mathbf{G}_{\mathrm{H}}^{T_\mathrm{s}} & \mathbf{0} & \mu_2 \mathbf{G}_{V_\mathrm{s}}^{T_\mathrm{s}} \\ \mathbf{0} & \mathbf{0} & \mu_3 \mathbf{G}_{V_\mathrm{s}}^{\mathrm{SW}} \\ \mathbf{0} & w_\mathrm{p}\mathbf{L}_{V_\mathrm{p}} & \mathbf{0} \\ \mathbf{0} & \mathbf{0} & w_\mathrm{s}\mathbf{L}_{V_\mathrm{s}} \\ \lambda_\mathrm{H}\mathbf{I} & \mathbf{0} & \mathbf{0} \\ \mathbf{0} & \lambda_\mathrm{p}\mathbf{I} & \mathbf{0} \\ \mathbf{0} & \mathbf{0} & \lambda_\mathrm{s}\mathbf{I} \end{bmatrix} \begin{bmatrix} \Delta\mathbf{H} \\ \Delta\mathbf{m}_\mathrm{p} \\ \Delta\mathbf{m}_\mathrm{s} \end{bmatrix} = \begin{bmatrix} \mu_1 \mathbf{d}^{T_\mathrm{p}} \\ \mu_2 \mathbf{d}^{T_\mathrm{s}} \\ \mu_3 \mathbf{d}^{\mathrm{SW}} \\ \mathbf{0} \\ \mathbf{0} \\ \mathbf{0} \\ \mathbf{0} \\ \mathbf{0} \end{bmatrix}, \tag{1}$$

where $\mathbf{G}_{\mathrm{H}}^{T_\mathrm{p}}$, $\mathbf{G}_{\mathrm{H}}^{T_\mathrm{s}}$, $\mathbf{G}_{V_\mathrm{p}}^{T_\mathrm{p}}$ and $\mathbf{G}_{V_\mathrm{s}}^{T_\mathrm{s}}$ are the sensitivity matrices of first P-arrival and S-arrival times with respect to hypocenter parameters, V_p, and V_s, respectively; $\mathbf{G}_{V_\mathrm{s}}^{\mathrm{SW}}$ is the sensitivity matrix of surface wave dispersion data with respect to V_s; $\mathbf{L}_{V_\mathrm{p}}$ and $\mathbf{L}_{V_\mathrm{s}}$ are the first-order smoothing matrices for the V_p and V_s models with weights of w_p and w_s, respectively; λ_H, λ_p, and λ_s are the damping parameters for hypocenter parameters, V_p, and V_s model parameters, respectively; $\Delta\mathbf{H}$, $\Delta\mathbf{m}_\mathrm{p}$, and $\Delta\mathbf{m}_\mathrm{s}$ are perturbations to hypocenter parameters, V_p, and V_s model parameters, respectively; and μ_1, μ_2 and μ_3 are relative weights for body wave P-arrival and S-arrival times and surface wave dispersion data, respectively. For simplicity in our study we set data weights μ_1 and μ_2 for P and S arrival time data to be equal. The damping parameters, smoothing weight parameters, and data weighting parameters are chosen by a combination of requiring a reasonable condition number (mainly controlled by the damping) and a trade-off analysis (examining the data weighting). We retain the same smoothing weight that was found to be optimal by Zhang *et al.* (2009). LSQR (Paige and Saunders, 1982) is used to solve the system of Eq. (1).

We note that there is a difference in the way the velocity structure is parameterized in the underlying body-wave versus surface-wave components of the joint inversion. For body-wave arrival times, the velocity structure is represented by the value at grid nodes, and interpolation is used to obtain the velocity value at any point. Thus, velocity is treated as a continuous function of position. In contrast, for the surface waves, velocities are defined in latitude-longitude cells and vertical layers such that the velocity is constant within each cell. To accommodate two different model parameterizations, we put the node in the center of each cell. For this study, the grid intervals are 0.0048° in latitude and 0.0044° in longitude, and vary from 0.5 to 3 km in depth (at $Z = -0.5$, 0, 0.5, 1.0, 2.0, 4.0, 7.0, and 10.0 km).

4. *Trade-off Curve and Inversion Results*

To explore specifically the effect of the joint inversion on the structural model, we keep all data and parameters constant except for the weighting of the body-wave equations, which we vary over several orders of magnitude, with the surface-wave weight kept fixed at 1. We note that the damping and smoothing we apply to stabilize LSQR and regularize the inversion is the same as that used by Zhang *et al.* (2009) in their body-wave only tomography study. We find that for weights below a value of 1 (i.e., equal weighting of body-wave and surface-wave equations), the misfit to both the body-wave and surface-wave data ceases to change, and above 100, the body-wave misfit remains constant. Thus, we consider the trade-off in data fit between body waves and surface waves in the range 1–100 for the body-wave weight (Fig. 4; Table 1). What we find is that there is a strong, smooth variation in data fit as we move from a weight of 1 to a weight of 100, with a "knee" in the curve near a weight of 20. Near this point, a small increase in the body-wave weight leads to a large increase in surface-wave misfit with little decrease in body-wave misfit. Conversely, a small decrease in the body-wave weight leads to a large increase in body-wave misfit with little decrease in surface-wave misfit. Thus, on this basis we tentatively identify a body-wave weight of 20 as optimal.

An independent way to estimate the proper relative weighting of the body-wave and surface-wave

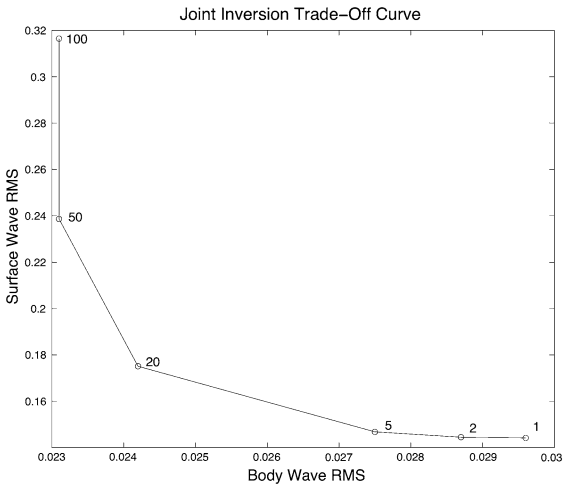

Figure 4
Plot of surface-wave data misfit (in km/s) versus body-wave data misfit (in s) in the joint inversion as a function of the body-wave weight (the surface-wave weight was kept fixed at 1). A body-wave weight of 20 is adopted as optimal

Table 1

Variance reduction for body-wave and surface-wave data as a function of the body-wave weight

Body-wave weight	Body-wave variance reduction (%)	Surface-wave variance reduction (%)
1	77.5	74.0
2	77.7	73.9
5	78.4	73.0
20	79.7	61.6
50	80.4	28.7
100	81.1	1.15

data is in terms of their relative data uncertainties. For the body-wave data, the average pick uncertainty is on the order of 0.02 s, based on the pick quality as estimated directly from the waveform data, which agrees well with the level of RMS misfit we obtain in the trade-off analysis (Fig. 3). Similarly, the surface-wave data uncertainty estimate of 10 % (Roux *et al.*, 2011) is consistent with the RMS misfit on the order of 0.2 km/s, given that the model velocities are mainly in the range of 1.5–3 km/s. The ratio of 10 between these two uncertainties is of the same order as the optimal weighting ratio of 20–1 from the trade-off curve in Fig. 4. This is analogous to the stochastic inverse (e.g., Aki *et al.*, 1977), for which the ratio of the a priori data variance to model variance is used as the damping factor in the least squares inversion.

Next, we compare the inversion model results for the nominal optimal body-wave weight (Fig. 5c) to those for low (Fig. 5a), moderately low (Fig. 5b), moderately high (Fig. 5d), and high (Fig. 5e) body-wave weights. Horizontal slices through the V_s models for the various cases are shown in Fig. 5 from 500 m above to 2 km below sea level, where the changes are greatest. Moving from the optimal (Fig. 5c) to the moderately low (Fig. 5b) and low (Fig. 5a) body-wave weight cases, the primary features remain present but the model amplitude variations are slightly reduced and smaller-scale features, especially those near the SAF, shrink or disappear. This indicates the lateral smoothing effect of the surface-wave data. Moving from the optimal (Fig. 5c) to the moderately high (Fig. 5d) and high (Fig. 5e) body-wave weight cases, the primary features still remain, but there is a substantial increase in the number and amplitude of the smaller-scale features. Given that the body-wave data misfit is reduced by only 4 % at the cost of a $\sim$35–80 % increase in the surface-wave data misfit, we interpret the higher-weight cases to indicate overfitting the noise in the body-wave data.

Roux *et al.* (2011) highlighted a "U-shaped" feature containing a low-velocity zone in their ambient noise model. We compare an iso-surface at the same V_s value of 2.5 km/s in our new model (Fig. 6a) to their original result (Fig. 6b). This steep-sided wedge of slow material corresponds to the sedimentary packages penetrated by the main SAFOD borehole. The joint inversion results reveal a greater depth and along-fault extent of this feature than the previous ambient noise only model.

We also note an area of strongly varying group velocity with frequency in the southeast part of our study area, near 35.97°, −120.50°, northeast of the SAF (Fig. 3). Here, group velocity drops from $\sim$2 km/s at 0.15 and 0.2 Hz to $\sim$1.2 km/s at 0.3 Hz. This is an area that has been observed to be anomalous in some previous studies. Zhang *et al.* (2009) found relatively high V_p here extending from $\sim$2 to 7 km depth from body-wave tomography, and Zhang *et al.* (2007) found the same area to be highly anisotropic ($\sim$4 %) from a tomographic inversion of shear wave splitting delays. Thus, it is not surprising to find it to be anomalous in terms of Love wave group velocity behavior as well.

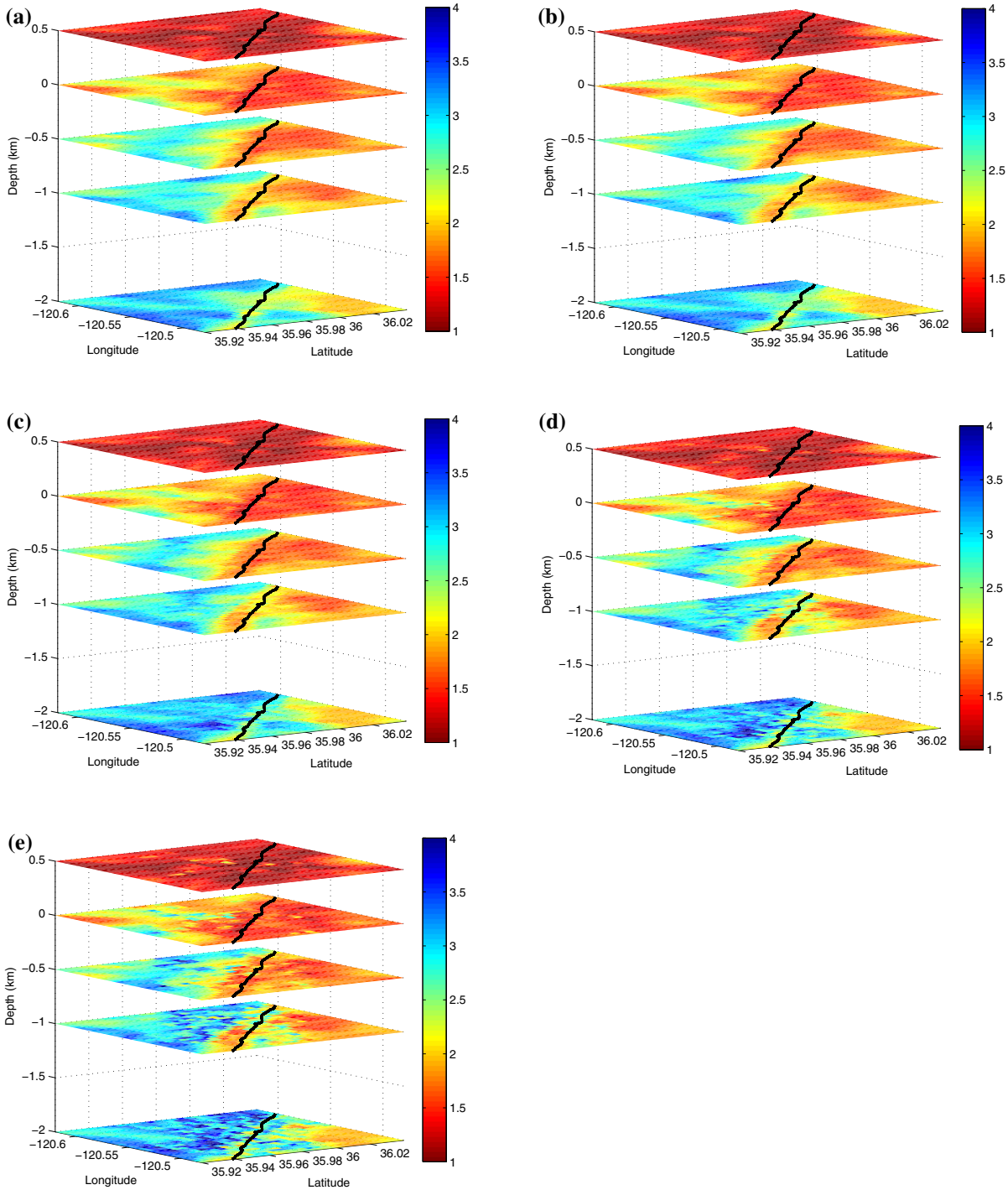

Figure 5

Comparison of velocity model results for different body-wave weights, showing *horizontal slices* at the depths of the shallow *grid nodes* (−0.5, 0, 0.5, 1, and 2 km depth relative to mean sea level). The weights used for the models that are shown: (**a**) 2, (**b**) 5, (**c**) 20, (**d**) 50, (**e**) 100. The *black line* is the SAF trace. The view is from the southeast

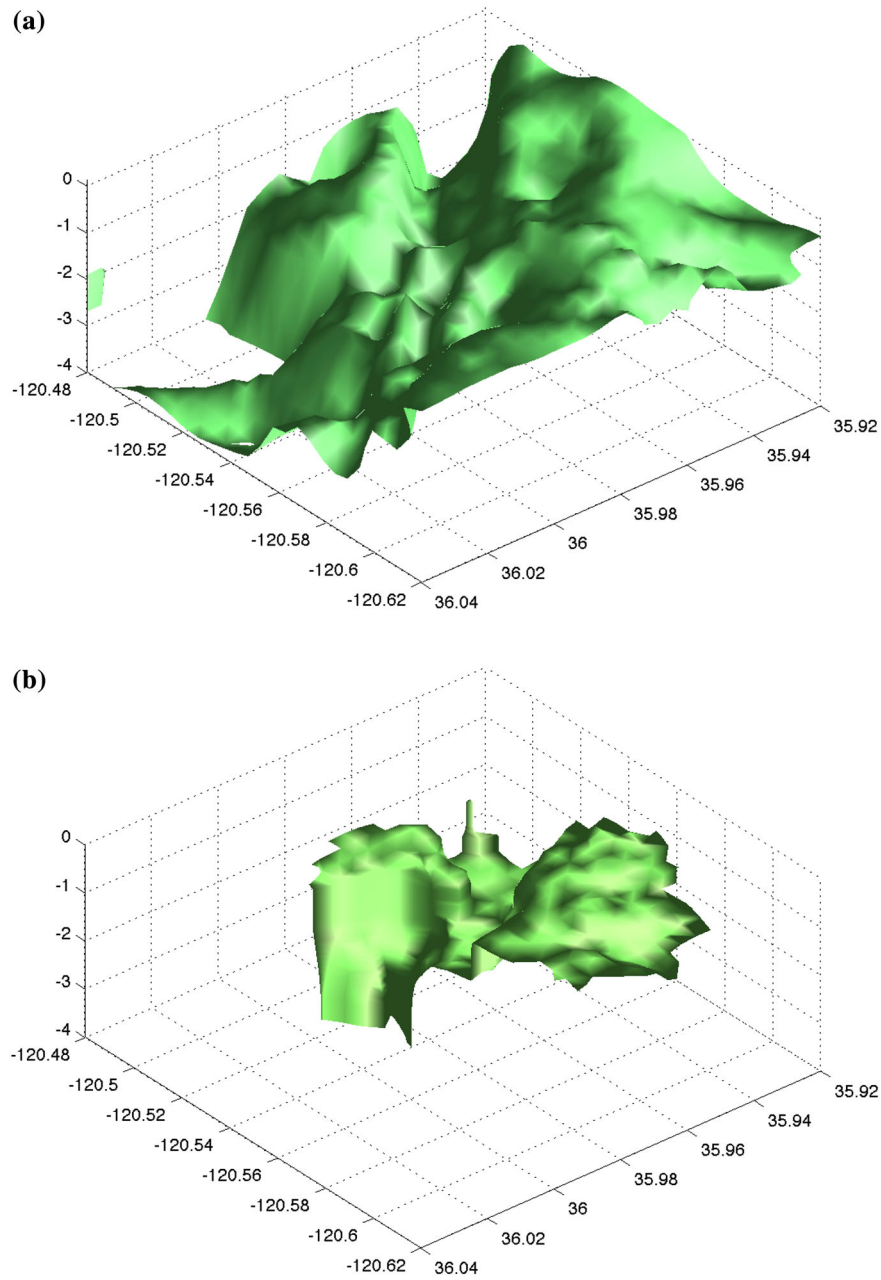

Figure 6
Iso-surface view of the 2.5 km/s V_s surface for (**a**) the weight of 20 model in Fig. 5 compared to (**b**) the same view from Roux *et al.* (2011). The view is from the northwest. Notice the deeper expression and longer extent of the "U-shaped" feature in the joint inversion model in (**a**)

5. *Discussion and Conclusions*

The joint inversion algorithm expressed by Eq. (1) has advantages compared to separate body-wave arrival time inversion and surface-wave dispersion inversion. Compared to the separate arrival-time inversion, the joint inversion V_s model is more strongly constrained by the combination of body-wave data and surface-wave data. Even though traditional surface-wave inversion typically only derives a V_s model, an updated V_p model is required at each iteration in order to compute the surface wave responses. In traditional

surface-wave inversions, this is generally accomplished by assuming a constant V_p/V_s ratio provided by the a priori model. In comparison, the joint inversion determines a more reliable V_p model from P-wave arrival times. As a result, the surface-wave responses are more accurate and the surface-wave data can be better used to invert for the V_s model.

The joint inversion results do not make significant changes to the main features found previously in the crust surrounding SAFOD. Rather, the joint inversion suppresses oscillatory features in the V_s model that do not make a significant change in the fit to the body-wave data. Adding the surface-wave constraints to the body-wave inversion leads to a simpler (smoother) V_s model that is able to fit both the body-wave and surface-wave data adequately.

Acknowledgments

We thank Yehuda Ben-Zion and Antonio Rovelli for organizing the 40th Workshop of the International School of Geophysics on "Properties and Processes of Crustal Fault Zones" in Erice, Sicily, which motivated the present work. We are grateful to two anonymous reviewers for their constructive comments, which we hope have led to substantial improvement of the manuscript. This research presented here was partly supported by the Chinese government's executive program for exploring the deep interior beneath the Chinese continent (SinoProbe-02), Natural Science Foundation of China under Grant No. 41274055, and Fundamental Research Funds for the Central Universities (WK2080000053). This research was also supported by DE-NA0001523 from the US Department of Energy.

References

Aki, K., A. Christoffersson, and E.S. Husebye (1977). *Determination of the three-dimensional structure of the lithosphere*, J. Geophys. Res., *82*, 277–296.

Aki, K., and P. G. Richards (1980). Quantitative Seismology: Theory and Methods, W. H. Freeman, San Francisco, CA, USA.

Bache, T. C., W. L. Rodi, and D. G. Harkrider (1978). *Crustal structures inferred from Rayleigh-wave signatures of NTS explosions*, Bull. Seismol. Soc. Am., *68*, 1399–1413.

Becken, M., O. Ritter, S. K. Park, P. A. Bedrosian, U. Weckmann, and M. Weber (2008), *A deep crustal fluid channel into the San Andreas Fault system near Parkfield, California*, Geophys. J. Int. *173*, 718–732.

Bennington, N., C. Thurber, and S. Roecker (2008), *Three-dimensional seismic attenuation structure around the SAFOD site, Parkfield, California*, Bull. Seismol. Soc. Am. *98*, 2934–2947.

Bennington, N., H. Zhang, C. H. Thurber, and Paul A. Bedrosian (in revision), *Joint inversion of seismic and magnetotelluric data in the Parkfield region of California using the normalized cross-gradient constraint*, Pure App. Geophys.

Ben-Zion, Y., and P. Malin (1991), San Andreas fault zone head waves near Parkfield, California. Science 251, 1592–1594.

Bleibinhaus, F., J. A. Hole, T. Ryberg, and G. S. Fuis (2007), *Structure of the California Coast Ranges and San Andreas Fault at SAFOD from seismic waveform inversion and reflection imaging*, J. Geophys. Res. *112*, B06315, doi:10.1029/2006JB004611.

Bucher, R. L., and R. B. Smith (1971). Crustal structure of the eastern Basin and Range Province and the northern Colorado Plateau from phase velocities of Rayleigh waves, in *The Structure and Physical Properties of the Earth's Crust*, Geophys. Monogr. Ser., vol. 14, edited by J. G. Heacock, pp. 59–70, AGU, Washington, D.C.

Catchings, R. D., M. J. Rymer, M. R. Goldman, J. A. Hole, R. Huggins and C. Lippus (2002), *High-resolution seismic velocities and shallow structure of the San Andreas Fault Zone at Middle Mountain, Parkfield, California*, Bull. Seismol. Soc. Am. *92*, 2493–2503.

Chavarria, J. A., P. Malin, R. D. Catchings, and E. Shalev (2003), *A look inside the San Andreas fault at Parkfield through vertical seismic profiling*, Science *302*, 1746–1748.

Du, W.-X., C. H. Thurber, and D. Eberhart-Phillips (2004), *Earthquake relocation using cross-correlation time delay estimates verified with the bispectrum method*, Bull. Seismol. Soc. Am. *94*, 856–866.

Eberhart-Phillips, D., and A. J. Michael (1993), *Three-dimensional velocity structure, seismicity, and fault structure in the Parkfield region, central CA*, J. Geophys. Res. *98*, 15,737–15,758.

Hole, J. A., R. D. Catchings, K. C. St. Clair, M. J. Rymer, D. A. Okaya, and B. J. Carney (2001), *Steep-dip imaging of the shallow San Andreas fault near Parkfield*, Science *294*, 1513–1515.

Hole, J., T. Ryberg, G. Fuis, F. Bleibinhaus, and A. Sharma (2006), *Structure of the San Andreas fault zone at SAFOD from a seismic refraction survey*, Geophys. Res. Lett. *33*, L07312.

Hole, J. A., and Zelt, B. C. (1995), *3-D finite-difference reflection traveltimes*, Geophys. J. Int. *121*, 427–434.

Julià, J., C. J. Ammon, R. B. Herrmann, and A. M. Correig (2000), *Joint inversion of receiver function and surface wave dispersion observations*, Geophys. J. Int. *143*, 99–112.

Korneev, V. A., R. M. Nadeau, and T. V. McEvilly (2003), *Seismological studies at Parkfield IX: Fault-zone imaging using guided wave attenuation*, Bull. Seismol. Soc. Am. *93*, 1415–1426.

Lees, J. M., and P. E. Malin (1990), *Tomographic images of P wave velocity variation at Parkfield, California*, J. Geophys. Res. *95*, 21,793–21,804.

Lewis, M. A., and Y. Ben Zion (2010), *Diversity of fault zone damage and trapping structures in the Parkfield section of the San Andreas Fault from comprehensive analysis of near fault seismograms*, Geophys. J. Int. *183*, 1579–1595.

Li, Y.-G., W. L. Ellsworth, C. H. Thurber, P. Malin, and K. Aki (1997), *Fault zone guided waves from explosions in the San Andreas fault at Parkfield and Cienega Valley, California*, Bull. Seism. Soc. Am. *87*, 210–221.

Li, Y.-G., and P.E. Malin (2008), *San Andreas Fault damage at SAFOD viewed with fault-guided waves*, Geophys. Res. Lett. *35*, L08304, doi:10.1029/2007GL032924.

Li, Y. G., P. C. Leary, K. Aki, and P. E. Malin (1990), *Seismic trapped modes in Oroville and San Andreas fault zones*, Science *249*, 763–766.

Li, Y.-G., J. E. Vidale, and E. S. Cochran (2004), *Low-velocity damaged structure of the San Andreas Fault at Parkfield from fault zone trapped waves*, Geophys. Res. Lett. *31*, L12S06, doi:10.1029/2003GL019044.

Michelini, A., and T.V. McEvilly (1991), *Seismological studies at Parkfield: I, Simultaneous inversion for velocity structure and hypocenters using cubic B-splines parameterization*, Bull. Seism. Soc. Am. *81*, 524–552.

Maceira, M. and C. J. Ammon (2009). *Joint inversion of surface wave velocity and gravity observations and its application to Central Asian basins shear velocity structure*, J. Geophys. Res. *114*, B02314, doi:10.1029/2007JB005157.

Paige, C. C., and M. A. Saunders (1982), *LSQR: An algorithm for sparse linear equations and sparse least squares*, ACM Trans. Math. Software *8*, 43–71.

Podvin, P. and I. Lecomte (1991), *Finite difference computation of traveltimes in very contrasted velocity models: a massively parallel approach and its associated tools*., Geophys. J. Int. *105*, 271–284.

Roecker, S., C. Thurber, and D. McPhee (2004), *Joint inversion of gravity and arrival time data from Parkfield: New constraints on structure and hypocenter locations near the SAFOD drill site*, Geophys. Res. Lett. *31*, L12S04.

Roecker, S., C. Thurber, K. Roberts, and L. Powell (2006), *Refining the image of the San Andreas Fault near Parkfield, California using a finite difference travel time computation technique*, Tectonophysics *426*, doi:10.1016/j.tecto.2006.02.026.

Roux, P., K.G. Sabra, P. Gerstoft and W.A. Kuperman (2005), *P-waves from cross-correlation of seismic ambient noise*, Geophys. Res. Lett. *32*, L19303.

Roueff A., P. Roux and P. Réfrégier (2009), *Wave separation in ambient seismic noise using intrinsic coherence and polarization filtering*, Signal Process. *89*, 410–421.

Roux, P. (2009), *Passive seismic imaging with directive ambient noise: Application to surface waves on the San Andreas Fault (SAF) in Parkfield*, Geophys. J. Int. *179*, 367–373.

Roux, P., A. Roueff and M. Wathelet (2011), *The San Andreas Fault revisited through seismic noise and surface-wave tomography*, Geophys. Res. Lett., *38*, L13319.

Saito, M. (1988), DISPER80: A subroutine package for the calculation of seismic normal mode solutions, in D. J. Doornbos (ed.), *Seismological Algorithms: Computational Methods and Computer Programs*, Academic Press, New York, pp. 293–319.

Takeuchi, H., and M. Saito (1972), Seismic surface waves, in *Methods of Computational Physics*, edited by B. A. Bolt, pp. 217–295, Academic, New York.

Tanimoto, T. (1991), *Waveform inversion for three-dimensional density and S-wave structure*, J. Geophys. Res., *96*, 8167–8189.

Tanimoto, T., S. Ishimaru, and C. Alvizuri (2006), Seasonality of particle motion of microseisms, *Geophys. J. Int. 166*, 253–266, doi:10.1111/j.1365-246X.2006.02931.x.

Thurber, C., S. Roecker, K. Roberts, M. Gold, L. Powell, and K. Rittger (2003), Earthquake locations and three-dimensional fault zone structure along the creeping section of the San Andreas fault near Parkfield, CA: Preparing for SAFOD, *Geophys. Res. Lett.* 30.

Thurber, C., S. Roecker, H. Zhang, S. Baher, and W. Ellsworth (2004), Fine-scale structure of the San Andreas fault zone and location of the SAFOD target earthquakes, *Geophys. Res. Lett. 31*, L12S02.

Unsworth M, and P. Bedrosian (2004) Electrical resistivity at the SAFOD site from magnetotelluric exploration, *Geophys. Res. Lett. 31*, L12S05, doi:10.1029/2003GL019405.

Unsworth M, P. Bedrosian, M. Eisel, G. Egbert, and W. Siripunvaraporn (2000) Along strike variations in the electrical structure of the San Andreas Fault at Parkfield, California, *Geophys. Res. Lett. 27*, 3021–2024.

Unsworth, M. J., P. E. Malin, G. D. Egbert, and J. R. Booker (1997), Internal structure of the San Andreas fault zone at Parkfield, California, *Geology 25*, 359–362.

Vidale, J. (1988), Finite-difference calculation of travel times, *Bull. Seis. Soc. Am. 78*, 2062–2076.

Waldhauser, F., and W. L. Ellsworth (2000). A double-difference earthquake location algorithm: method and application to the northern Hayward Fault, California, *Bull. Seism. Soc. Am.* 90, 1353–1368.

Wu, J., J. A. Hole, and J. A. Snoke (2010), Fault zone structure at depth from differential dispersion of seismic guided waves: evidence for a deep waveguide on the San Andreas Fault, *Geophys. J. Int. 182*, 343–354.

Zhang, H., and C. H. Thurber (2003), Double-difference tomography: The method and its application to the Hayward Fault, California, *Bull. Seism. Soc. Am. 93*, 1875–1889.

Zhang, H., and C. Thurber (2005). Adaptive mesh seismic tomography based on tetrahedral and Voronoi diagrams: Application to Parkfield, California, *J. Geophys. Res. 110*, B04303.

Zhang, H., and C. Thurber (2006). Development and applications of double-difference tomography, *Pure App. Geophys. 163*, 373–403, doi:10.1007/s00024-005-0021-y.

Zhang, H., Y. Liu, C. Thurber, and S. Roecker (2007), *Three-dimensional shear-wave splitting tomography in the Parkfield, California Region*, Geophys. Res. Lett. *34*, L24308. doi:10.1029/2007GL03195.

Zhang, H., C. Thurber, and P. Bedrosian (2009), Joint inversion for V_p, V_s, and V_p/V_s at SAFOD, Parkfield, California, *Geochem. Geophys. Geosyst. 10*, Q11002, doi:10.1029/2009GC002709.

Zhang, H., C. Thurber, D. Shelly, S. Ide, G. Beroza, and A. Hasegawa (2004), High-resolution subducting slab structure beneath Northern Honshu, Japan, revealed by double-difference tomography, *Geology 32*, 361–364.

(Received September 14, 2013, revised February 17, 2014, accepted February 19, 2014)